

We are IntechOpen, the world's leading publisher of Open Access books Built by scientists, for scientists

6,100

Open access books available

149,000

International authors and editors

185M

Downloads

Our authors are among the

154

Countries delivered to

TOP 1%

most cited scientists

12.2%

Contributors from top 500 universities



WEB OF SCIENCE™

Selection of our books indexed in the Book Citation Index
in Web of Science™ Core Collection (BKCI)

Interested in publishing with us?
Contact book.department@intechopen.com

Numbers displayed above are based on latest data collected.

For more information visit www.intechopen.com



Chapter

Lead-Free Perovskite and Improved Processes and Techniques for Creating Future Photovoltaic Cell to Aid Green Mobility

Rira Kang, Tae-ho Jeong and Byunghong Lee

Abstract

Perovskites material is in the spotlight as photovoltaic device due to their optical and physical properties. In a short period of time, this organic-inorganic perovskite can achieve about energy conversion efficiencies of 25.6% by anti-solvent and spin-coating based process. In addition, ambipolar carrier transport properties of perovskite materials open up new directions for the high-efficiency thin-film solar cells. Despite its attractive properties in solar cell application, concerned about device stability and the use of lead compounds ($APbX_3$, A = a cation X = halide) with toxicity cause the potential risk for the human body and environment issue. Therefore, the use of a new classed structural materials with intrinsic stability and beneficial optoelectronic properties can be considered as a start of the next chapter in perovskite device. This chapter is structured into two major parts: In section 1, we introduce more stable class of perovskite, A_2SnX_6 , where Sn is in the 4+ oxidation state. A detailed discussion on the ramifications of material structure and chemistry-related challenges is presented for solution processing, along with careful characterization. In section 2, we talk about the direction of development for perovskite materials to be a next chapter of energy source for a green mobility.

Keywords: perovskite, AMX_3 , A_2MX_6 , lead-free perovskite, $CsSnI_3$, Cs_2SnI_6 , coating technique, impedance analysis, vacuum evaporation

1. Introduction

1.1 Lead Free Perovskite Materials

The continual development in efficiency of lead-halide-based perovskites has yielded phenomenal success with efficiencies above 25% [1]. To date, however, there have been few reports of scalable solution or vapor processing techniques being applied to the deposition of perovskite films with nontoxicity and stability. It is

apparent that the path toward commercialization of solution-processed perovskite solar cells requires the development of fabrication protocols compatible with high-volume roll-to-roll or sheet-fed processing techniques. Although the use of lead in perovskite is expected to have many human and environmental issues in the future, these factors are not currently being considered due to the battle for solar cell efficiency. This research trends make the future of perovskite solar cell darker. Therefore, the most important key to the commercialization of perovskite solar cells is the development of lead-free structured materials with competitive solar cell efficiency.

1.2 Tin-based perovskite

Tin of a group 14 element with comparable ionic radii is currently considered as one of the best candidates to replace lead compounds due to its meaningful electrical and optical properties [2]. Completely lead-free perovskite solar cells based on $\text{CH}_3\text{NH}_3\text{SnI}_3$ were reported in 2014 yielding efficiencies of 5.23% [3] and 6.4% [4] with the suppression of Sn^{4+} accomplished through ultrahigh purity starting materials, fastidious synthesis, and glove box device fabrication protocols. In terms of optical bandgap calculated by Shockley-Queisser for the highest efficiency, $\text{CH}_3\text{NH}_3\text{SnI}_3$ ($E_g \sim 1.3$ eV) is considered the ideal materials ($E_{g, \text{ideal}} \sim 1.35$ eV). However, relatively lower efficiency, the poor long-term stability, and low reproducibility of these films caused by the tendency for Sn to get oxidized are insufficient to replace this material with lead-based perovskite [4]. To improve power conversion efficiencies (PCEs) as inhibiting the oxidation of Sn^{2+} to Sn^{4+} , $\text{CH}_3\text{NH}_3\text{Sn}_x\text{Pb}_{1-x}\text{I}_3$, which is mixture compounds of Sn and Pb, is reported [5]. Mixtures containing about $x = 0.25$ of Sn ($\text{CH}_3\text{NH}_3\text{Sn}_{0.25}\text{Pb}_{0.75}\text{I}_3$) showed $\sim 7.4\%$ of the best efficiency [6]. Further improvement (PCE $\sim 10.1\%$) was demonstrated as adding Cl, which show a better film coverage, effective exciton dissociation, and charge transport [7].

1.3 CsSnI₃-typed perovskite

With Kanatzidis's group, we introduce p-typed CsSnI_3 semiconductor, which is a distorted three-dimensional perovskite structure that crystallizes in the orthorhombic $Pnma$ space group at room temperature (RT) (**Figure 1(a)**) [11]. The Sn^{2+} center sits in a distorted octahedral environment with six I^- anions, resulting in stereochemically inactive so-called $6s^2$ lone pair of electrons. The $\{\text{SnI}_{6/2}\}^-$ octahedra condense to form a three-dimensional framework via corner-sharing with the Cs^+ countercations residing at 12 coordinate interstices within the network made by eight $\{\text{SnI}_{6/2}\}^-$ octahedra. This structure exhibits direct bandgap properties of ~ 1.3 eV and very high hole mobility of $\mu_h = 585 \text{ cm}^2 \text{ V}^{-1} \text{ s}^{-1}$ with p-type conduction behavior at RT. Thermoelectric power measurements gave positive Seebeck coefficients over the entire temperature range with linear dependence on temperature, suggesting p-type conduction (**Figure 1(b)**). The hole mobility can be estimated from the electrical conductivity using the equation $\mu_h = \sigma p^{-1} e^{-1}$ (where μ_h is the hole mobility, σ is the electrical conductivity, p is the hole concentration, and e is the electronic charge). The calculated value is close to that obtained from the Hall effect measurements. Therefore, this compound can be considered as being an excellent candidate material for replacing lead-based perovskite. In 2012, a related inorganic CsSnI_3 perovskite was used as a hole conductor by combining the ruthenium dyes, reaching 8.5% efficiency [12]. From these properties and initial works, the field of p-typed perovskite material has attracted great attention. After these initial works, the field of perovskite-based solar

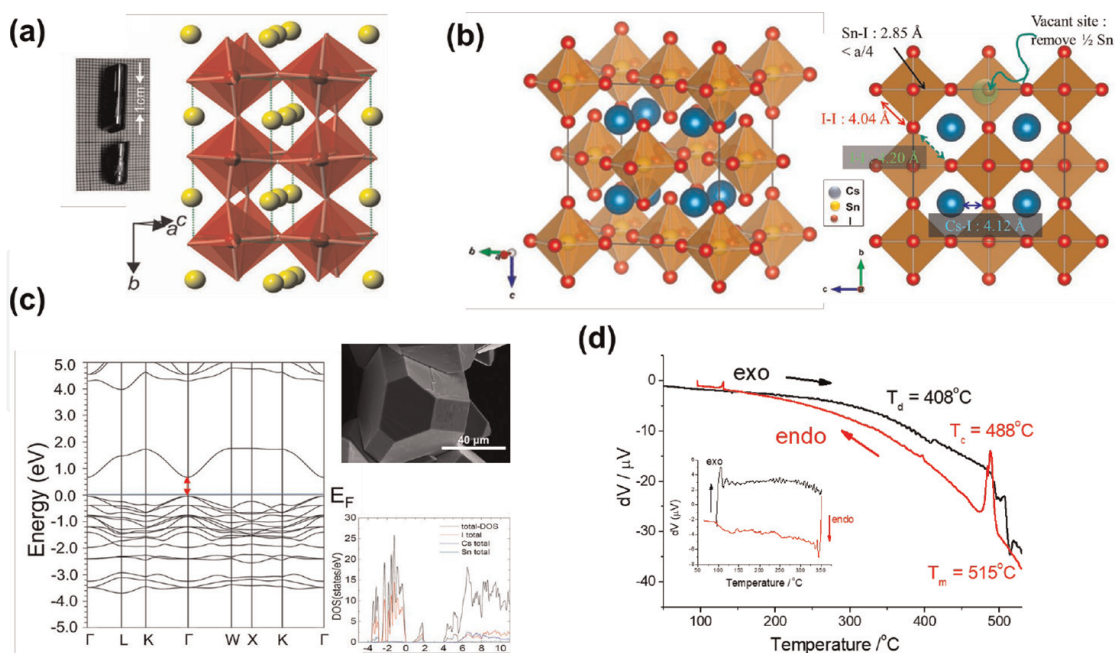


Figure 1.

(a) Distorted three-dimensional perovskite structure of CsSnI₃ at RT. red polyhedron, {SnI_{6/2}}⁻: Yellow, Cs. (b) Crystal structure of Cs₂SnI₆ from the VESTA program. (c) DTA and graphs for Cs₂SnI₆ for temperature maxima of 400–600°C. reprinted from [8–10].

cells has literally exploded, with extremely exciting very recent results. CsSnI₃ successfully also was demonstrated as light absorber [13]. The high photocurrent densities of more than 22 mAcm⁻² can be attained by utilizing CsSnI₃ due to its favorable bandgap, optical properties, and low exciton binding energies (BEs) (18 meV) [14]. Nonetheless, an improvement of open-circuit voltage (~0.24 V) is still required [15]. Also, the fabrication of tin-based *ASnI₃* perovskite cells is highly unstable in the ambient due to the tendency for Sn to get oxidized, and its easy oxidation creates Sn⁴⁺ that originates a metal-like behavior in the semiconductor which lowers the photovoltaic performance [5, 16]. Therefore, a clear improvement on the stability remains an objective.

1.4 Cs₂SnI₆-typed perovskite

A new class of perovskite variants *A₂BX₆* would be attractive candidates because *B* in *A₂BX₆* is expected to be the +4 oxidation state upon assumption of the A⁺ and X ion states, which would lead to a stable structure in air and moisture [8]. It can be inferred that the electronegativity and ionic radii play an important role to be the stable structure, the lattice parameters of which are determined by the competition between the ionic Coulomb and exchange correlation contributions [17]. This typed crystals are *Fm-3m* space group with four formula units in one unit cell, and it is chemically bonded from the Coulomb interactions between the particular ions [17]. In this crystalline structure, 12-fold of each monovalent cation A coordinates (in the unit of the lattice constant) are (0.25, 0.25, 0.25), each tetravalent cation B is sixfold coordinated by the halogen ions (*x*, 0, 0), where *x* is somewhat different (varying around 0.2) for different structures. From optical band structure, halogen ions are located in the upper valence band and the bottom of conduction bands is formed dominantly by the cationic *s*-states. Usually incorporation of the d-transition metal ions (in the case of

doped crystals) gives additional localized d -states, which form the bottom of the conduction bands.

1.5 Characteristics of Cs_2SnI_6 perovskite

1.5.1 Structural properties

The α -phase of Cs_2SnI_6 crystallizes into the face-centered-cubic (fcc) K_2PtCl_6 type with the space group $Fm\bar{3}m$ (the antiferroite structure) and the lattice parameter a of 11.6276 (9) [16]. The unit cell is configured of four $\{\text{SnI}_6\}^{2-}$ octahedra at the corners and the face centers and eight Cs^{2+} cations at the tetragonal interstitials. (see **Figure 1(b)**) Alternatively, Cs_2SnI_6 can be regarded as a defective variant of the AMX_3 structure type similar to those of CsSnI_3 , $\text{CH}_3\text{NH}_3\text{SnI}_3$ and $\text{CH}_3\text{NH}_3\text{PbI}_3$ compounds, in which the $\{\text{SnI}_6\}$ octahedra connect to each other by sharing their corners. In Cs_2SnI_6 , half of the octahedral Sn atoms are missing creating discrete $\{\text{SnI}_6\}^{2-}$ octahedra. The compound is therefore a molecular salt and contains Sn^{4+} rather than Sn^{2+} in CsSnI_3 . This accounts of the stability of the material. After the half of the Sn atoms are removed, the $\{\text{SnI}_6\}^{2-}$ octahedra shrink slightly, leading to the smaller $\text{Sn} - \text{I}$ bond length (2.85 Å) [17] in Cs_2SnI_6 than that in CsSnI_3 (3.11 Å) [9] as well as the smaller intraoctahedral $\text{I} - \text{I}$ bond length (4.04 Å) than that of interoctahedral $\text{I} - \text{I}'$ bond lengths (4.20 Å).

1.5.2 First-principles electronic band structure of Cs_2SnI_6

The self-consistent full-potential linearized augmented plane wave method (LAPW) within density functional theory (DFT) and the generalized gradient approximation (GGA) of Perdew, Burke, and Ernzerhof for the exchange and correlation potential and WIEN2k program is used for electronic structure calculations [18–23]. The modified Becke-Johnson exchange potential is also employed for bandgap correction [24]. From these calculations, Cs_2SnI_6 estimate a direct bandgap of ~ 1.3 eV at the Γ point comprising filled $\text{I}-5p$ orbitals and empty hybrid $\text{I}-6p/\text{Sn}-5s$ orbitals for the valence band maximum (VBM) and conduction band minimum (CBM), respectively (**Figure 1(c)**). The valence and conduction bands are surprisingly well dispersed in energy, for a molecular $\{\text{SnI}_6\}^{2-}$ salt compound, with ~ 1 eV and ~ 0.5 eV bandwidth, respectively. Such a band configuration appears to justify the remarkably high electron and hole mobility of pristine Cs_2SnI_6 .

1.5.3 Electrical properties

From Hall effect measurements, electrical resistivity of a pressed polycrystalline pellet of Cs_2SnI_6 by annealing at 200°C shows a reasonably low value of $\sim 100 \Omega\cdot\text{cm}$. The electron carrier concentration is measured to be on the order of $\sim 1 \times 10^{14} \text{ cm}^{-3}$ by RT and $\approx -2.6 \times 10^3 \mu\text{V}/\text{K}$ of the Seebeck coefficient. Plus, electron mobility of the pristine bulk material that behaves as an n-type semiconductor shows about $310 \text{ cm}^2/\text{V}\cdot\text{s}$. Interestingly, with doping Sn^{2+} (as SnI_2) in Cs_2SnI_6 , p-typed semiconductor behavior can be observed ($\sim 1 \times 10^{14} \text{ cm}^{-3}$ of a nearly identical carrier concentration and $S \approx 1.9 \times 10^3 \mu\text{V}/\text{K}$ of the Seebeck data). The hole mobility and resistivity of the p-type Cs_2SnI_6 show $\sim 42 \text{ cm}^2/\text{V}\cdot\text{s}$ and $780 \Omega\cdot\text{cm}$, respectively. Although electron mobility level of p-type Cs_2SnI_6 is lower than that of the $\text{CH}_3\text{NH}_3\text{PbI}_3$ perovskite, it still preserves a considerable hole mobility [5, 16]. And, we

can clearly understand the ambipolar nature of Cs_2SnI_6 from these characteristics of both n- and p-type behavior.

1.5.4 Thermal properties of Cs_2SnI_6

The thermal stability of Cs_2SnI_6 is assessed by differential thermal analysis (DTA). The temperature maximum in each scan was varied progressively by a 100°C increment between 400°C and 600°C (**Figure 1(d)**). The melting point T_m was determined to be at $\sim 515^\circ\text{C}$, but X-ray diffraction suggests that the melting proceeds through partial decomposition to CsI (mp = 621°C , bp = 1277°C) and SnI_4 (mp = 143°C , bp = 348.5°C). It is not clear at which temperature the decomposition occurs, but it can be tentatively assigned to the reversible process occurring at $T_d \sim 410^\circ\text{C}$. The further thermal properties of Cs_2SnI_6 powder are analyzed by thermal gravimetric analysis (TGA) and differential scanning calorimetry (DSC) measurements. For the TGA data, the drastic weight loss onset occurs at 269°C , which is attributed to the beginning of the decomposition of Cs_2SnI_6 to SnI_4 and CsI from the perovskite frameworks. Nearly 44% weight loss between 270°C and 350°C of Cs_2SnI_6 is observed. In general, DSC measurement can be helped to understand a sublimation and a decomposition process for Cs_2SnI_6 . The DSC curve exhibits two small endothermic peaks at 200°C and 308°C . Both TGA and DSC results also confirm that the Cs_2SnI_6 crystal is relatively good stability and nonexplosive character. In order to verify this behavior, three independent samples of Cs_2SnI_6 are prepared starting from pristine, solution precipitated material. The first sample consists of the 'as made' fresh material, whereas the other two have been annealed at 350°C and 550°C , respectively, in evacuated ampoules. In agreement with the DTA and TGA data, the material obtained from 350°C annealing remains unchanged, whereas the treatment at 550°C results in a molten solid ingot which is, however, contaminated with orange crystals of SnI_4 . High-resolution powder X-ray diffraction using synchrotron radiation confirms the decomposition of Cs_2SnI_6 to SnI_4 and CsI above 410°C . This is accompanied by a relative loss of crystallinity, as judged by the loss of diffraction intensity and the relative broadening of the reflections.

1.6 Cs_2SnI_6 formation processes

Deposition of perovskite films by spin coating process with anti-solvent is a highly common method employed in perovskite photovoltaics research [25]. This method is a good way on a laboratory scale, but it is not suitable for large-area or mass production process. Here, we introduce a new two-step process (a CsI deposition in Step 1 by e-spraying process and vaporization of SnX_2 or SnX_4 in Step 2) method of Cs_2SnX_6 (X = halide) compounds film formation. In earlier research, a series of experiments describe how we have optimized our two-step solution processes for synthesizing iodosalts $\text{Cs}_2\text{SnI}_{6-x}\text{Br}_x$ thin films to achieve suitable properties as solar photon absorbers for light to charge conversion [10]. This paper is well explained what the importance of Step 1 is and how to apply this. As another approach for making better thin films, we adopted the method suggested by Saparov et al. [26] that Vapor SnI_4 treatment is a thermally activated chemical reaction and the reaction temperature is independent of the SnI_4 temperature needed to establish the vapor concentration. The schematic representation of the experimental vaporized step was illustrated in **Figure 2(a)**. The as-made CsI film prepared by e-spraying and excess SnI_4 powder was placed in a sealed glass container with the different positions (the center: CsI

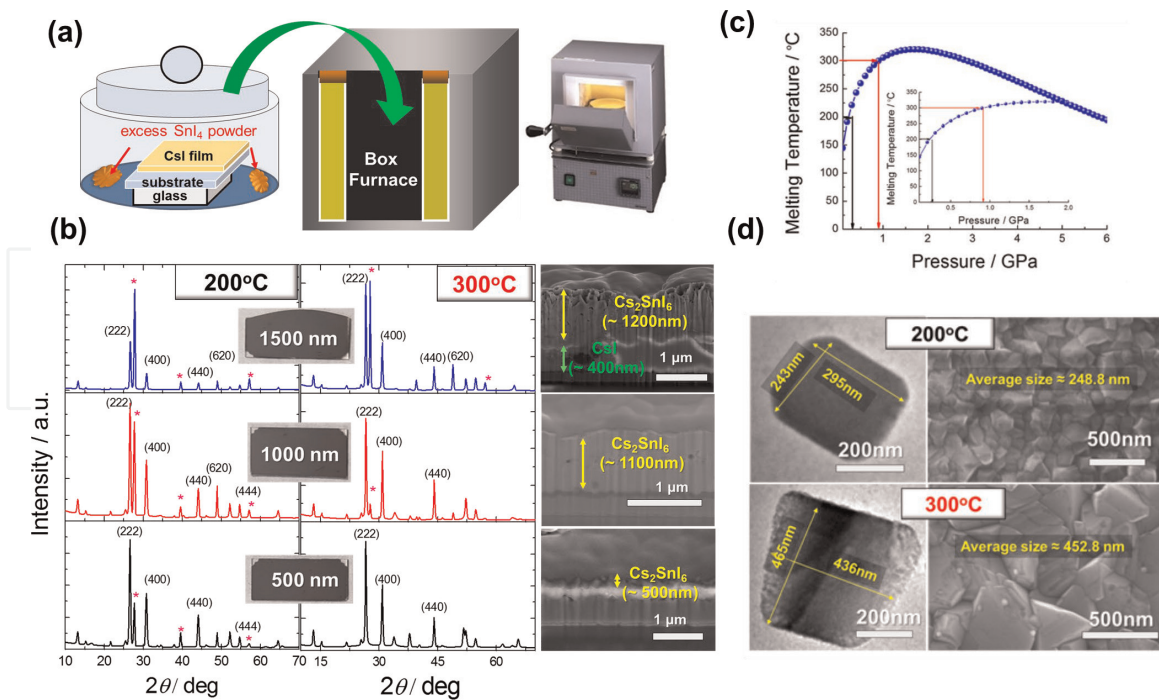


Figure 2.

Vaporized technique as a step 2 process: (a) illustration showing vaporizing procedure; (b) XRD analysis and cross-sectional image for the different film thickness; (c) vaporized condition for SnI₄ powder; and (d) morphological study from SEM and TEM analysis for 200°C and 300°C for 1 hour.

film, the edge: excess SnI₄ powder) and rapidly heated to the reaction temperature (25–200°C or 300°C) for 1 hour in a box furnace at a rate of 10°C/min. In our first observation, even if the films show very smooth surfaces, SnI₄ vaporization condition at 200°C for 60 min is not enough to fully convert the Cs₂SnI₆ crystal because of the existence of the main peaks of CsI film at all the thickness appears at 2θ = 27.6° (see **Figure 2(b)**). Therefore, we choose a different condition based on the ground of the work of Fuchizak [27, 28]. In more detail, at the initial stage of the experimental research into the melting behavior, Simon's equation is used:

$$\frac{p}{p_0} = \left(\frac{T_m}{T_0} \right)^{c_s - 1} \quad (1)$$

where T_0 and p_0 are the values at the reference state, T_m is the melting temperature at pressure p , and c_s is a constant. This substitution is believed not to cause any significant issues. Second, the Kechin melting curve equation is discussed. This equation was derived from

$$\frac{d \ln T_m}{dp} = \frac{\Delta V}{\Delta H} = \frac{\Gamma_m}{K_m} \quad (2)$$

Here, ΔV and ΔH denote the changes in volume and enthalpy upon melting, and hence the first equality merely states the Clapeyron-Clausius relationship. K represents the isothermal bulk modulus [27]. The subscript "m" denotes that the quantities are calculated from a melting curve, or more precisely, along a solidus. Thus, Γ_m and K_m are considered as the asymptotic quantities of Γ and K evaluated in

the solid state. Because only a solid state is involved in the assessment of the second equality, it was referred to as a “one-phase” approach in contrast to the first equality, called a “two-phase” approach. Γ is defined by:

$$\Gamma = \frac{-d \ln T}{dp} = 2 \left(\gamma - \frac{1}{3} \right) \quad (3)$$

where γ is Grüneisen's parameter, and the latter equality is evolved from Lindemann's melting law. The quite intriguing point in Kechin's treatment for Eq. (2) is to employ the Padé approximation to express the RHS and to obtain the solution:

$$\frac{T_m}{T_0} = \left(1 + \frac{p}{a} \right)^b e^{-cp} \quad (4)$$

when $L = M = 1$ was chosen in the Padé approximant. The constants, a , b , and c , are expressible in terms of the original thermodynamic quantities contained in Eq. (2) as follows:

$$a = \frac{\Delta H_0}{\Delta H'_0} = \frac{K_{m0}}{K'_{m0}}$$

$$b = \frac{\Delta V_0}{\Delta H'_0} + ac = \frac{\Gamma_{m0}}{K'_{m0}} + a \quad \text{and} \quad c = \frac{\Delta V'_0}{\Delta H'_0} = -\frac{\Gamma'_{m0}}{K'_{m0}}$$

where a prime denotes a pressure derivative, and the subscript “0” means that the quantity is estimated at $p = p_0 (\simeq 0)$. When $c = 0$, Eq. (3) can be simplified to Eq. (1). Eq. (3) is “almighty” in that it can capture an unusual melting curve with a maximum at $p_{\max} = b/c - a$.

However, Eq. (3) was used only as a fitting guide, and no examination was attempted to demonstrate the fitted parameters on the basis of Eq. (4). Here, we are simply fitted to Eq. (3), treating a , b , and c as fitting parameters with “best-fit” value. The overall aspect of the fit is not bad, but the actual melting curve seems to break more abruptly near 1.5 GPa, beyond which it becomes almost flat, with a slight maximum at about 3 GPa (**Figure 2(c)**). Based on this information, we test a different sets of condition Cs_2SnI_6 film produced by vaporized SnI_4 treatment with the different thicknesses. XRD analysis and morphology study for the different thickness can be seen in **Figure 2(b)**. All of the diffraction peaks are indexed as Cs_2SnI_6 with the space group, $\text{Fm-}3\text{m}(225)$ (JCPDS #04-016-3227). This experimental study shows that the complete reacted 500-nm-thick Cs_2SnI_6 film can be obtained after SnI_4 vapor exposure at 300°C for 1 hour. However, when the thickness is over 500 nm, a CsI impurity peak started to appear. Thus, to remove unreacted CsI, a different treatment condition is needed (e.g. we can also confirm the completely converted Cs_2SnI_6 film at 300°C for 2 hour). Furthermore, we obtain the large Cs_2SnI_6 crystal for the 300°C cases. From SEM top-view images in **Figure 2(d)**, the 300°C treated sample has shown an increased grain size with diameters of 453 ± 35 nm, while the diameters of 200°C treated sample are in the range of 240 ± 58 nm. The TEM images are used to further examine the crystal size. The sizes for 200°C and 300°C treated Cs_2SnI_6 films are estimated to be 269 ± 24 nm and 450 ± 16 nm, respectively, which are consistent with the SEM observations. The grain size (D) of two samples is also independently calculated from XRD data using Scherrer formula [29]. The (222) peak at $2\theta = 26.5^\circ$ is fitted to estimate the grain size of Cs_2SnI_6 . The 222 peak gives an estimate of the average

crystallite size only in the *ab*-plane direction. As expected, the average grain size increases only slightly after 1 h of annealing at 300°C ($D = 58.80 \pm 0.2$ nm) compared with the 200°C treated samples ($D = 52.21 \pm 0.6$ nm). The increased grain size correlates with an improved film conductivity. This improvement is mainly provided by the carrier mobility being enhanced from $1.94 \text{ cm}^2/(\text{V}\cdot\text{s})$ for the 200°C treated film to $11.24 \text{ cm}^2/(\text{V}\cdot\text{s})$ for the 300°C treated Cs_2SnI_6 film, and to a lesser extent by the carrier concentration that increases slightly from $1.57 \times 10^{15} \text{ cm}^{-3}$ to $4.89 \times 10^{15} \text{ cm}^{-3}$ at a film thickness of 1.5 μm . This experimental research indicates that bulk electrical conductivity reduces with the decreasing grain size. The electrical property change can be attributed to fewer boundaries impeding electron mobility in the 300°C treated films [30].

The optical properties of Cs_2SnI_6 film prepared by the vaporized technique can be also seen in **Figure 3(a)**. The film formed vaporized condition followed the same optical (1.6 eV) and electrical properties are quite similar to the literature results [26]. This reason can be understood by the following experiment: X-ray photoemission spectroscopy (XPS) and ultraviolet photoelectron spectroscopy (UPS) measurements of the Cs_2SnI_6 film produced by the different methods were performed for compositional and chemical states analysis. The presence of Cs, Sn, and I elements is clearly discernible (**Figure 3(b)**). The binding energies of 619.7 eV and 631.2 eV are indicative of I3d bonded to Cs3d at binding energies (BEs) of 725.1 and 739 eV, in good agreement of result for CsI peak [31]. In the case of the Sn compound, the main binding energies of $\text{Sn}3d_{5/2}$ and $\text{Sn}3d_{3/2}$ obtained from solution method are about 488 eV and 496 eV, respectively, attributed to Sn^{4+} state (see **Figure 3(b)** middle column). Interestingly, in the case of the vaporization method, the main binding energy at 487.3 eV can be assigned to Sn^{2+} , leading to intrinsic defects and instable form, with a nominal formula $\text{Cs}^+_2\text{Sn}^{2+}(\text{I}_6)^{4-}$ [26, 32–34]. The vaporization of a system of tetrahedral MX_4 groups linked through vertices (silica-like structure) is accompanied by a reduction in the coordination number of the metal, in some instances to polymeric species which dissociate to monomers at higher temperature [35]. Thus, the formation of the Sn^{2+} oxidation states can be explained by halogen transfer during the high-temperature process [36–38]. The position of energy levels for occupied states can be also determined by UPS analysis. (**Figure 3(b)** right column) The BE of the HOMO onset of Cs_2SnI_6 film prepared from the different method is determined by the intersect of the linear extrapolation of the leading edge of the HOMO peak and the straight background line. The Fermi level in most of the presented spectra is fixed at zero binding energy, and all the measured positions are

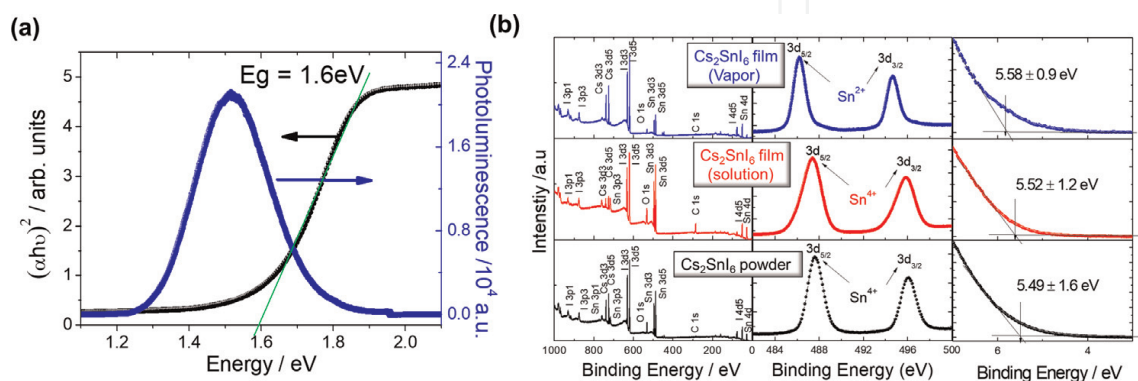


Figure 3.

(a) The optical absorption and PL analysis at 1000 nm thickness prepared by the vaporized technique at 300°C for 1 hour, and (b) XPS and UPS analysis for Cs_2SnI_6 prepared from the different technique.

referred with respect to the Fermi level. The HOMO onset of Cs_2SnI_6 powder and film from solution method are observed to be 5.52 ± 1.2 eV, while for the vapor method they are measured to be 5.58 ± 0.9 eV. The downshift of HOMO level with increasing bandgap can be considered by the distortion of crystal from the Sn^{2+} state. The different oxidation state can affect not only crystal structure account of the different ionic radius of Sn^{2+} (102 pm) and Sn^{4+} (69 pm) but also has a profound influence on a number of physical properties [39, 40]. The Sn^{2+} compounds are expected to have distortions of their bonded configurations because of the influence of their nonbonded pair of electrons, while the $5s^0p^0$ configuration of the Sn^{4+} ion should give regular octahedral coordination for tin in ionic lattices. The bond length of Cs_2SnI_6 can be seen in **Figure 1(b)** [17, 41]. The missed half of Sn atom brought the Sn-I length (2.89 Å) closer to the actual value (2.85 Å), while estimated Sn-I length of Sn^{2+} was about 3.22 Å. The incongruous Sn-I length leads to the distortion of Cs_2SnI_6 . From Goldschmidt tolerance factor (t), we can simply understand the stability and distortion of Cs_2SnI_6 crystal with Sn^{2+} and Sn^{4+} oxidation state [42]. The tolerance factor is calculated from the ionic radius of the atoms [43]. A tolerance factor of 0.71–0.9 originates from a distorted perovskite structure with tilted octahedra. In the case of the tolerance factor is higher (>1) or lower (<0.71), perovskite phase cannot be formed. This rule made for oxide perovskite, but the trend is still valid for pero-halide perovskite materials structure. The calculated tolerance factor of Sn^{2+} oxidation state can be estimated by 0.9012 (from SPuDS software program), while the maximum t achievable of Sn^{4+} oxidation state is 0.998. The decreased t value of the Sn^{2+} oxidized state indicates that the network of corner-shared SnI_6 octahedral will tilt in order to fill space, causing a less stable structure.

Figure 4 illustrated the electronic structure of Sn^{2+} state $\text{Cs}_2\text{Sn}^{2+}\text{I}_6^{4-}$ and Sn^{4+} state $\text{Cs}_2\text{Sn}^{4+}\text{I}_6^-$ presented by Xiao et al. [33, 41]. The chemical bonding nature and the origin of the bandgap in Cs_2SnI_6 can be understood by DFT calculations for some hypothetical structure. The qualitatively arranged group of electronic structure on the energy scale can be seen in **Figure 4(a)**. The electron structure on an isolated [36] octahedron (i.e. $\{\text{I}_6\}^0$ cluster) is firstly displayed. The 18 I 5p orbitals of the $\{\text{I}_6\}$ octahedron are split to seven groups, following by the energy eigenvalues at the Γ point and the group theory. The six radial I 5p orbitals split into three groups of a_{1g} (I-I bonding) and e_g & t_{1u} (I-I antibonding). The 12 tangential I 5p orbitals form 4 triply

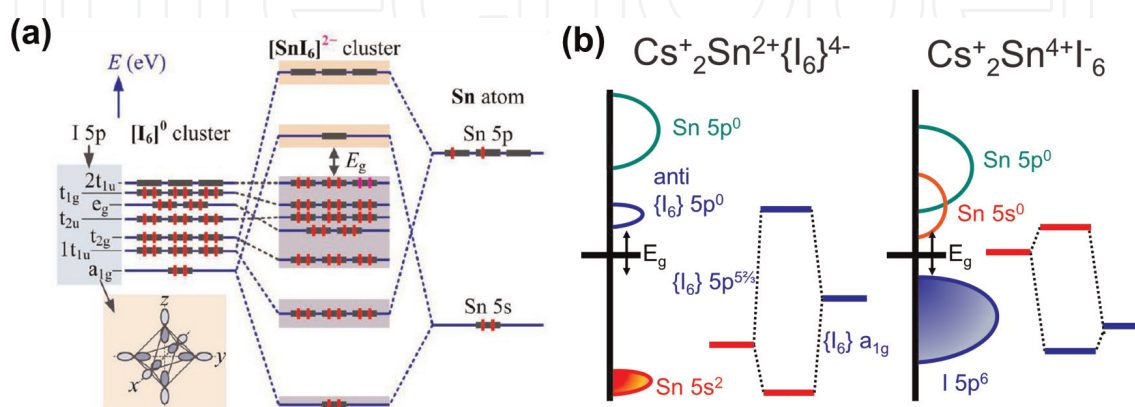


Figure 4. (a) Total and projected DOSs of qualitative interaction diagram for the $\{\text{I}_6\}^0$ cluster, the $\{\text{SnI}_6\}$ cluster, and the $\{\text{SnI}_6\}$ sublattice models. The orbital are qualitatively arranged on the energy scale. A schematic illustration of $\{\text{I}_6\}^0$ a_{1u} orbital: (b) schematic electronic structure for the different state Cs_2SnI_6 . Reprinted form [41].

degenerated groups of $1t_{1u}$ & t_{2g} (I-I bonding) and t_{2u} & t_{1g} (I-I antibonding). By adding a Sn atom and two electrons (transferred from the two Cs atoms, which is ionized to Cs^+ in Cs_2SnI_6) into the $\{I_6\}$ octahedron, the electronic structure of a $\{SnI_6\}^{2-}$ octahedron cluster is obtained. Therefore, the main difference between the +2 and +4 oxidation state is the Sn 5s orbital position. The unoccupied Sn 5s orbital at the $Cs^+_2Sn^{4+}I_6^-$ state is contributed to the conduction band maximum (CBM). However, the calculated $Cs^+_2Sn^{2+}I_6^{4-}$ state had the fully occupied Sn 5s orbital and I 5p-Cs 6s antibonding CBM state. The +2 oxidation state of Sn has deeper VBM, and it can be explained by its wide bandgap. Using the one-micron-thick Cs_2SnI_6 film produced by solution and vapor as a photosensitizer, we fabricated three different series of solar cells structure: (a) nanoporous $TiO_2/Cs_2SnI_6/Au$; (b) nanoporous $TiO_2/Cs_2SnI_6/Spiro-OMeTAD/Au$; and (c) nanoporous $TiO_2/Cs_2SnI_6/LPAH/Au$. As shown in the SEM cross section, a nanoporous TiO_2 layer with interpenetrating layer of Cs_2SnI_6 is placed as the next layer. A selected HTM layer is next deposited followed by the evaporation of a thin Au contact layer. Three different series of HTM layers prepared from solution and vapor processes are shown in **Figure 5(a)**. The bottom of SEM images is also displayed in their band diagrams. The $J-V$ curves for each of the device structure are plotted in **Figure 5(b)**, along with a table showing their characteristics. For configuration a. and d., we observed a substantial short circuit in the device of both solution- and vapor-processed samples. For configuration e., the vaporized samples show the best performance in typed cells ($\eta = 0.505\%$), while the solution-processed solar cell shows the best performance ($\eta = 0.177\%$) in the configuration c.. The overall improved PCE at the vaporized process is attributed to their

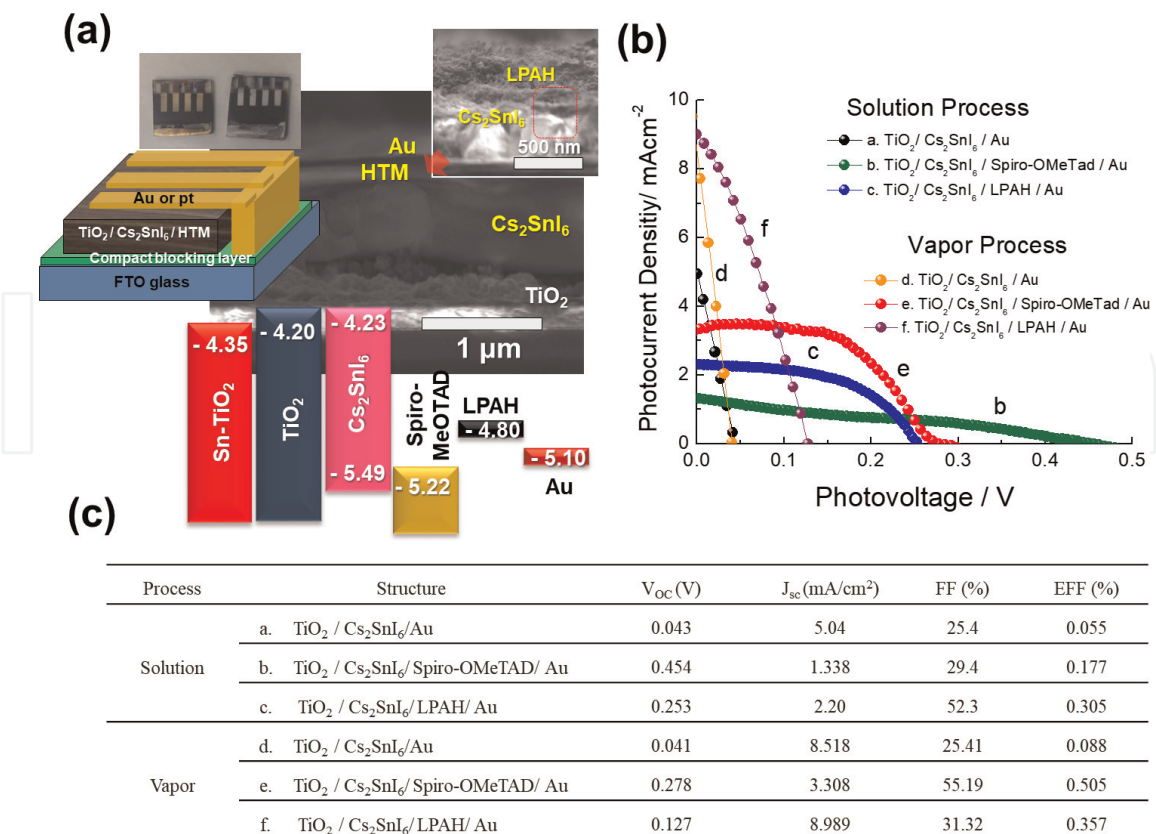


Figure 5.

(a) Schematic and cross-sectional images of a Cs_2SnI_6 film device (bottom: band alignment diagram) (b) $J-V$ curves for different structures and device performance as described in the table above.

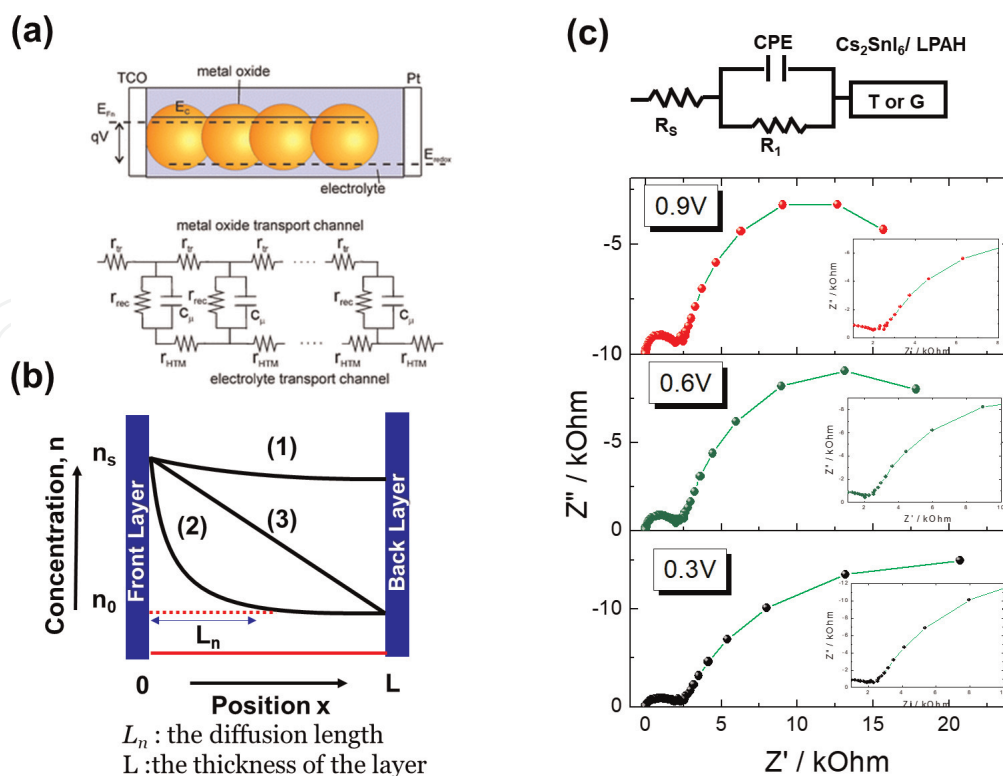
smooth surface, but still a low efficiency at 0.5%. However, it should be noted that large-effective-surface-area polyaromatic hydrocarbon (LPAH) can be dispersed well in alcoholic solvent (such as ethanol and isopropanol) without any polymer binder or surfactants [44]. Interestingly, the LPAH suspension with isopropanol also shows long-term dispersion stability. We believe that our findings make it possible to use this unique carbon nanostructural material as HTM material. In order to prove the effectiveness of LPAH, we tested that the case of a methylammonium lead iodide (MAPbI₃) thin film can lead to high-efficiency device. (This book will not cover it).

Operating mechanisms of the Cs₂SnI₆-based solar cells have raised a number of questions. The optimization and further improvement of a new material require a deep knowledge of the working principles of this photovoltaic device. In order to understand the effectiveness for photosensitizer, the charge transfer process is studied by two different tools such as electrochemical impedance spectroscopy (EIS) and femtosecond transient optical spectroscopy (i.e. TAS and time-resolved PL (TRPL) spectroscopy) for measuring accumulation of a photogenerated charge and the diffusion length (L_D) [45–47].

1.6.1 Impedance analysis

In earlier reports, dye-sensitized solar cells (DSSCs) have been successfully modeled by equivalent circuit elements, which have helped to elucidate the roles of internal interfaces as well as device components [48, 49]. From simulated model, average charge carrier lifetime, electronic densities of states, and charge carrier concentrations can be calculated. However, in the single-electrode system like BHJ organic photovoltaic devices or perovskite solar cell, the different impedance model is applied due to their geometrical difference [50–52]. Herein, we consider the properties of the impedance associated with diffusion coupled with recombination [45, 46, 51]. As seen in **Figure 6(a)**, electron energy diagram of an electron-transporting materials (specially, nanostructured metal oxide, TiO₂, SnO) in contact with a hole-conducting material (or redox medium), displaying the electrochemical potential of electrons E_{Fn} (Fermi level), when a voltage V is applied to the substrate, and assuming that conduction band energy (E_c), is stationary with respect to the redox level, E_{redox} . The equivalent circuit (transmission line model, TL) for a small periodic ac perturbation contains the resistance for electron transport throughout the metal oxide nanoparticles, r_{tr} ; the resistance in the hole-transporting medium (hole or ion conduction) r_{HTM} ; the recombination resistance at the metal oxide/HTM interface, r_{rec} ; and the chemical capacitance for charge accumulation in the metal oxide particles, C_μ . The TL pattern related to the carrier transport at lower frequency which is due to a coupling of capacitance with recombination is demonstrated by a straight line. (The extension of the straight line cuts the semicircle at low frequencies).

The model corresponding to the reflecting boundary condition is shown in **Figure 6(a)** and contains three main elements. The first is the chemical capacitance (C_μ), which makes C_μ dominate the total capacitance at sufficient forward bias. The C_μ is related to the variation of the electron Fermi level in the TiO₂ caused by the variation of the electron density as a function of the voltage. The fitting of TL allows to separate the two resistive parameters, for an active film of area A and layer thickness L . The second is the recombination resistance, R_{rec} , and the third is the transport resistance R_{tr} , that is reciprocal to the carrier conductivity, σ and the conductivity relates to the free electrons diffusion coefficient, as:


Figure 6.

(a) Electron energy diagram and general TL (b) concentration at the left boundary with concentration in the diffusion-recombination model. Curve represents the case (1) $L_n \gg L$, (2) $L_n \ll L$ (3) long diffusion length with strong recombination at the back contact (c) the equivalent circuit used to fit the experimental data and impedance spectroscopy characterization. Reprinted from [46, 51].

$$R_{rec} = \frac{\tau_n}{C_\mu}, R_{tr} = \frac{L}{A\sigma}, \sigma = \frac{C_\mu D_n}{L}$$

It is important to remark the following property:

$$R_{tr} = \left(\frac{L}{L_d}\right)^2 R_{rec} \text{ and } L_d = \left(\frac{R_{rec}}{R_{tr}}\right)^{1/2} L$$

The diffusion length (L_d) is also obtained from electron diffusion coefficient, D_n , and electron lifetime τ_n , as $L_d = \sqrt{D_n \tau_n}$ and indicates the average distance that generated or injected electrons travel before recombining. Influence of L_d of the carrier distribution in forward bias under dark conditions is illustrated in **Figure 6(b)**. For reflecting boundary (1) of long diffusion length, the carrier profile is nearly homogeneous. For short diffusion length (2), a gradient of carriers for the size of diffusion length is built from the injection point, and the rate of recombination at the back surface becomes another important factor. Finally, if the rate is large (3), excess carriers cannot remain at this boundary, and a gradient for the size of the semiconductor layer is built. **Figure 6(c)** shows a set of the characteristic impedance spectra pattern obtained for the $\text{Cs}_2\text{SnI}_6/\text{LPAH}/\text{Au}$ at different applied voltages in the working conditions under 0.1 sun illumination. For all the spectra, an arc is observed at high frequencies related to the transport in $\text{Cs}_2\text{SnI}_6/\text{LPAH}$. At low frequencies, for samples, the classical feature of a transmission line, TL, discussed earlier is clearly visible. The TL pattern is defined by a straight line, associated with the carrier

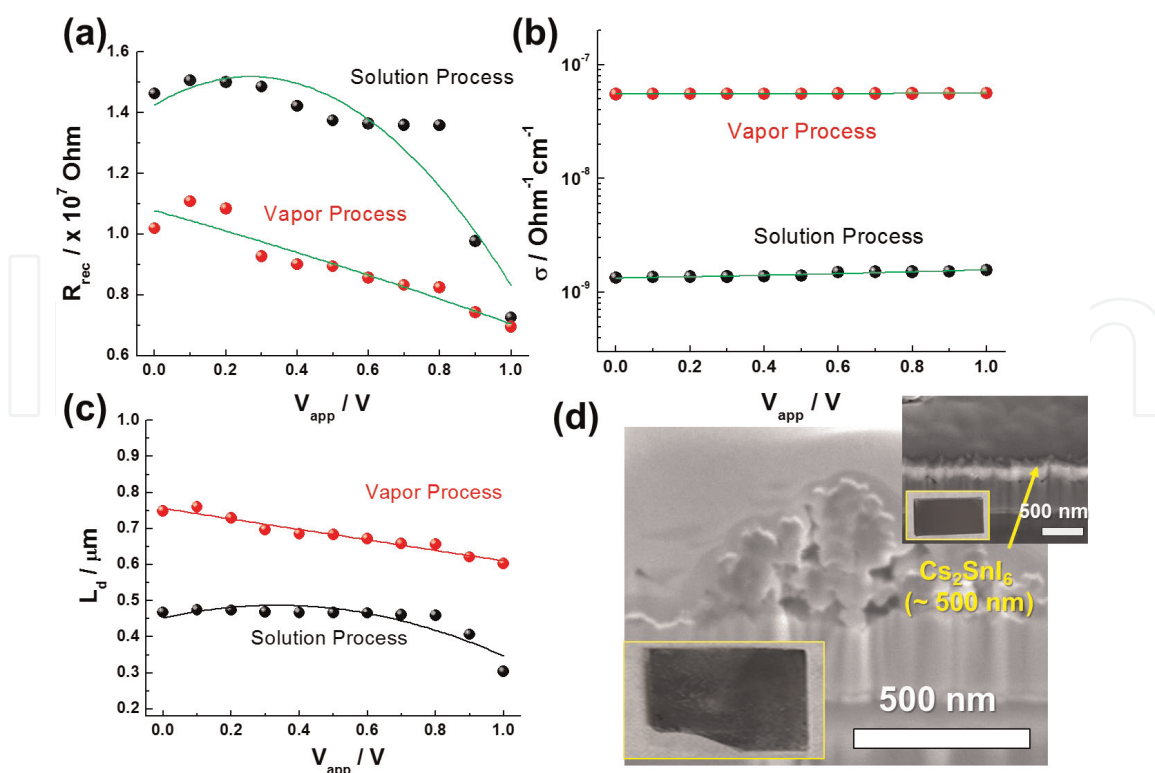


Figure 7. Transport and recombination parameters vs. voltage: (a) recombination resistance, R_{rec} ; (b) conductivity of active layer considering the geometric cell area; (c) diffusion length; and (d) cross-sectional SEM images of solution-processed film (inserted in (top) vapor processed film (bottom) photo image) for $\sim 500 \text{ nm}$ thick Cs_2SnI_6 film.

transport, followed by an arc at lower frequency, which is due to a coupling of capacitance with recombination. The fitting results are presented in **Figure 7**.

Important information about the recombination in the solar cell is contained in the recombination resistance, R_{rec} , and the transport rate is related to conductivity, σ . In the case of thin film ($\sim 500 \text{ nm}$), a Cs_2SnI_6 film produced by vaporized process exhibits two orders of higher conductivity, while it displays lower R_{rec} at comparable potentials (higher recombination rate) compared with Cs_2SnI_6 film from solution process. Therefore, diffusion length (L_d) of vapor-processed Cs_2SnI_6 film ($\sim 0.76 \mu\text{m}$ at low voltage) is increased by as much as 65.2%, compared with solution-processed film ($\sim 0.46 \mu\text{m}$ at low voltage). This reason can be considered as improved Cs_2SnI_6 film quality. For example, solution-processed Cs_2SnI_6 film shows the rough film with pinhole surface because of the loss during converting crystal formation such as being washed away by dropping SnI_4 alcoholic solvent (**Figure 7(d)**). The light absorption properties of Cs_2SnI_6 film can be determined by absorption coefficient. Materials with strong absorption coefficients more readily absorb photons, which excite electrons into CB. Thus, knowing the absorption coefficients of materials aids engineers in determining which material to use in their solar cell designs. The calculated coefficient (α) of $7.11 \times 10^2 \text{ cm}^{-1}$ at 550 nm measured for Cs_2SnI_6 film (at $\sim 500 \text{ nm}$) is about two order lower than that of $1.32 \times 10^4 \text{ cm}^{-1}$ at 550 nm for MAPbI_3 film (at $\sim 400 \text{ nm}$) [53]. Although a wider absorption spectrum of Cs_2SnI_6 film is benefit from light absorption, a low α must be improved to be the efficient photosensitizer. The higher α can be obtained by increasing film thickness developed. For example, α is estimated to be $1.7 \times 10^3 \text{ cm}^{-1}$ and $8.5 \times 10^3 \text{ cm}^{-1}$ at 550 nm for 1000 nm and 1500 nm Cs_2SnI_6 film, respectively, which indicates that α of thicker film is an order of magnitude higher than that of thinner film. However, from calculated diffusion length and the

experimental limitation for a completely reacted Cs_2SnI_6 film, we conclude that about $1.0 \mu\text{m}$ thick is the best condition for the efficient solar cell. Unlike aforementioned results, the opposite behavior, i.e. increased transport rate and decreased recombination rate at thicker film, can be observed due to the existence of CsI impurity at vapor process. Consequentially, in the case of about $1.0 \mu\text{m}$ thick, solution-processed Cs_2SnI_6 film shows longer diffusion length ($1.5 \mu\text{m}$) than that of vapor process ($0.78 \mu\text{m}$). This result indicates solution process is more favorable technique for thicker layer film. However, vapor-processed Cs_2SnI_6 film shows a high photocurrent and increased performance regardless of CsI impurity (leading to decrease L_d) compared with solution method. Therefore, our group believes that a completely converted or single-crystalline Cs_2SnI_6 film over $1.5 \mu\text{m}$ thick under well-controlled vapor process leads to the outstanding solar performance.

1.6.2 Femtosecond time-resolved transient absorption spectroscopy

The further photo-induced charge transfer processes can be confirmed by the excited-state dynamics measured from femtosecond transient absorption (fs-TA) spectroscopy [54]. In the case of over 800 nm , the totally black colored Cs_2SnI_6 film has a problem to transmit light through the samples. Therefore, $>500 \text{ nm}$ of Cs_2SnI_6 film is used for this study. **Figure 8** presents the normalized ground-state fs-TA spectra of solution and vapor-processed Cs_2SnI_6 film on Al_2O_3 ($<100 \text{ nm}$, Aldrich). Samples are excited with 600 nm , and 10 nJ laser pulses are used with the same

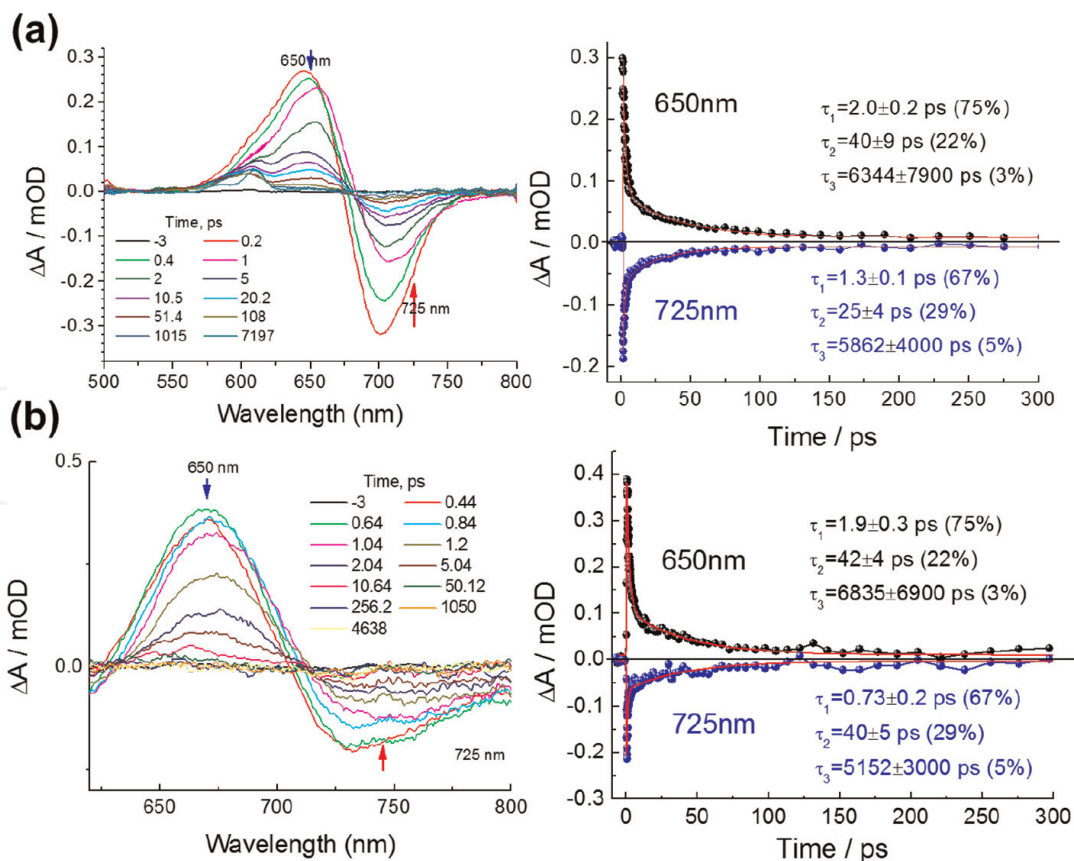


Figure 8. Femtosecond transient absorbance spectra with white light continuum probe and pulsed fs laser excitation at 600 nm and 10 nJ laser pulses are used with the same spectrum spanning from 500 to 800 nm . Dynamics extracted at 650 nm (black) and 725 nm (blue) for (a) solution and (b) vapor process for a two-step Cs_2SnI_6 film.

spectrum spanning from 500 to 800 nm. Both samples show two main features: a positive band in the range of 600–680 nm and broad negative band peaked at 680–800 nm. The broad positive band is resulted in the superposition of a ground-state bleaching (GSB) and simulated emission (SE) due to the close resemblance to the spectra of steady absorption and photoluminescence; the negative spectral feature is assigned to photo-induced absorption of excited state (PIA) as bleaching transitions from valence band to a conduction band [55]. The peak at 590 nm in case of solution is considered a noise peak caused by the uncovered Cs_2SnI_6 layer film defect. In the global analysis procedure, the decay-associated spectra with time constant probing at 630 nm and 725 nm are plotted in **Figure 8(c)** and **(d)**.

The completely reacted and covered Cs_2SnI_6 film shows three time constants of 1.9 ps (74%), 42.4 ps (21%), and 6835 (5%) at 650 nm as well as 0.73 ps (73%), 40.5 ps (21%), and 5152 ps (6%) at 725 nm, while a solution-processed Cs_2SnI_6 film reveals three time constants of 2.02 ps (75%), 40.9 ps (22%), and 6344 ps (3%) at 650 nm and 1.31 ps (67%), 38.4 ps (29%), and 5862 ps (5%) at 725 nm. The fast component for these samples is accounted for charge carrier trapping at grain boundaries of perovskite. We assign the longer time component (τ_2) to electron injection into glass. This long-lifetime component, not resolved in this work, is most likely electron-hole recombination [56–59]. For 650 and 725 nm, the small differences observed between solution ($\tau_{2,650\text{nm}} = 40.9$ nm and $\tau_{2,725\text{nm}} = 38.4$ nm at solution process, while for vapor process, $\tau_{2,650\text{nm}} = 42.4$ nm and $\tau_{2,725\text{nm}} = 40.5$ nm). The small differences observed for both samples are not significant enough to draw any conclusion regarding the electron injection process. The further experiment for this measure did not progress by the difficulty in the sampling. For example, in electric field deposition system, a conductive substrate is prerequisite for making a continuous and homogeneous thin film. However, for fs-TA spectroscopy analysis, nonconductive substrate is favorable to clarify the electron transfer dynamics of material itself. Therefore, in this thesis, fs-TA is no longer used. In spite of possible charge dynamic properties charge injection and the similar diffusion length ($L_d \approx 0.8 \mu\text{m}$ at ~ 500 nm) of Cs_2SnI_6 film compared with MAPbI_3 -based solar cell ($L_d \approx 1 \mu\text{m}$), our initial finding showed very low device efficiencies. Nevertheless, we were encouraged because the device operated as a photosensitizer even when the conduction band energy level between TiO_2 and Cs_2SnI_6 layer is nearly the same. A possible solution to this problem can be sought in bandgap tuning, and this can be achieved i) through the modification of the electron-transporting layer and ii) using an appropriate $\text{Cs}_2\text{SnI}_{6-x}\text{Br}_x$ absorption layer. These two approaches are discussed in the next paper.

2. Toward scalable fabrication of perovskite solar cells for mobility

Over the last decade, various support policies for electric vehicles (EVs) have been established in key markets, facilitating a major expansion of EVs models. But the challenge remains enormous such as driving range improvement and electricity production for charging EVs. Therefore, there are many efforts to increase the mileage of EVs. The use of solar energy would theoretically be the ideal fuel for EVs. In addition, significant fiscal incentives were provided for cars equipped with solar roofs (see IRC Section 30D(g)(1)(A)). Thus, major manufacturers expressed great interest in vehicle-intergraded solar cells. Still, the limited coverage area and efficiency of crystalline silicon-based solar cells make it difficult to have been active in a car application. Recently, Sono Motors, Lightyear one, and Mercedes-Benz presented the concept of

the electric concept sedan with a range of 620 miles (~ 1000 km) by increasing the solar panel area such as the roof, hood, and trunk. However, unlike stationary solar cells, mobile one requires higher standards (e.g. climatic tests such as temperature, humidity, and sun, and mechanical tests such as shock, drop, and scratch resistance are conducted for pedestrian safety.) Hyundai (Sonata and IoniQ5) and Toyota (Prius) successfully launched solar-roof-integrated cars from the lamination technique of the panoramic sunroof.

Hyundai Motor Group continues to study solar roofs, hoods, and trunks with different requirements. Although the development of next-generation solar cells has been underway for a long time, unfortunately, silicon is still a primary material for commercial solar cells. As mentioned earlier, the mobile car with a limited area requires a new material solar cell capable of higher efficiency (above 30%) and flexibility for easy application. Here, we deal with perovskite cells (PVCs) for mobility only from the point of view of the fabrication method. Perovskite is regarded as one of the next-generation materials that can overcome or create synergy with c-Si. Many researchers and company have suggested fabrication methods on a lab scale, not in the mass production stage. In this section, we show the scalable fabrication method of PSCs, considering that different integration technologies are required depending on the parts in the car.

2.1 Solution-based fabrication of perovskite solar cells

There are representative PSCs manufacturing companies. They present various fabrication methods and strategies for the commercialization of perovskite (**Table 1**). The latest trends in development in schools and companies, along with increasing interest in PSCs, are described on website [60]. Solution-based fabrication of PSCs is similar to organic solar cells (OSCs) and organic light-emitting diode (OLED). In the case of OSCs, relatively high efficiency ($\sim 18.2\%$) and mass production processes have been successfully researched in Kolon Industry [61]. Still, it has not been expanded due to the poor stability of organic materials. Moreover, the operating life issues of solution-processed OLED panels compared with the vacuum-processed device make it still an uncommon technique. Similar to these two devices, fabrication methods of PSCs have been developed. Similar to these two devices, PSCs are expected to have the same problem. To avoid these problems, we will briefly review the perovskite coating process.

Company	Manufacturing target	Technique.	Performance claims
Oxford PV (UK)	Rigid perovskite/Si tandem	PVD	29.8% @ 1.12cm ² (tandem)
Microquanta (China)	Rigid glass-backed perovskite cells.	?	17.3% @ 17.3cm ² (module).
Saul Tech. (Poland)	Printed flexible, lightweight, perovskite-only cells (niche application, e.g. IoT device)	Inkjet printing	25.5% with a small area
Panasonic (Japan)	Rigid perovskite cells. (comparable c-Si)	Inkjet printing	16.1% @ 802 cm ² (module)
Toshiba (Japan)	lightweight modules for rooftops (LCOE of 7yen/kWh)	Meniscus coating	15.1%, @ 703. cm ² (flexible)

Table 1.
Comparison of some companies commercializing perovskite.

2.1.1 Spin coating technique

It has been widely used to fabricate small cells less than 0.1 cm^2 and large module with area of 100 cm^2 as well [62]. The main advantage of this technique is simple, has high reproducibility, and is easy to control a nanoscale film thickness. For perovskite application, one-step and two-step of spin coating method are used. For one-step spin coating, the mixed precursor solution (organic halide salts and lead halide salts are dissolved in commonly used solvent such as DMF and DMSO) is spin-coated under layer (charge-transporting layer). In order to prevent incomplete crystallization during on-step process, the two-step method including so-called anti-solvent engineering was introduced [63]. This method has been widely used to produce high-quality film because it rapidly induces supersaturation, but the anti-solvent method cannot guarantee uniformity over a large area as the wet film is washed out. Additionally, since this method causes materials loss and stains with large-area coating, it is necessary to develop a method to replace this technique.

2.1.2 Meniscus coating (slot die and blade) coating

The term “meniscus coating” is the translation of a meniscus across the surface of a substrate as the solution is spread through a coating head or blade. These coating methods include slot die coating and blade coating. These coating can be applied in both sheet-to-sheet (S2S) and roll-to-roll (R2R) (see **Figure 9(c)** and **(d)**). Using R2R process, the material loss rate is less than 1% and high productivity can be expected [64]. The film thickness of the meniscus coating can be governed by the precursor solution concentration, the coating speed, and the gap distance between the blade or coating head and the substrates. A blade or a coating head moves across a surface or vice versa in the case of R2R. The blade spread predispensed ink, and the slot-die spread ink through a microfluidic metal die. They form it into a wet film. Compared with the spin coating, the solvent evaporation rate of meniscus-coated perovskite film is relatively slow, which promotes the growth of larger crystals. Because of the difficulty in controlling crystallization of perovskite film only by the natural drying, additional mechanical (e.g. preheating substrate [65] and gas blowing [66]) and chemical treatment (e.g.. anti-solvent [67]) are required. The former two cases are

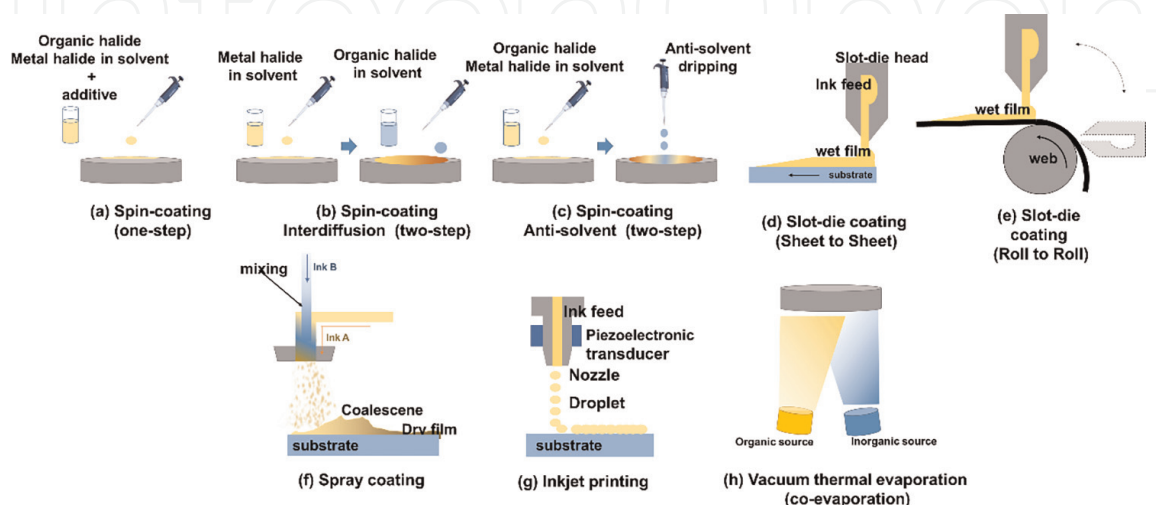


Figure 9. Schematic of solution-based fabrication and vacuum thermal evaporation (co-evaporation).

possible through modified coating equipment. The latter, the two-step method with anti-solvent, has been commonly used in spin coating, as discussed before. However, this method is difficult to be transferred from spin coating to meniscus coating due to its narrow time window. In this regard, solvent engineering of perovskite precursor ink is required to enable a one-step method. Depending on the existence of an ink reservoir, the slot die coating is more useful than a blade coating for scale-up [68]. Regardless of substrate type, all slot-die coating is still difficult due to materials and device structure restrictions (see **Table 2**). Still, the current intermediate results of these coating are likely to be the first solid step toward future manufacturing of the PSCs cells.

2.1.3 Spray coating

As a low-temperature coating technology, spray coating with low cost, high volume, rapid manufacturing, and low material loss rate is the most widely used technique. Spray coating uses relatively low-concentration “inks.” This process can be divided into four stages: *i*) the generation of the ink droplets, *ii*) the transport of the droplets to the substrate, *iii*) the coalescence of the droplets into a wet film, and *iv*) the drying of the thin film (**Figure 9(f)**) [68]. In recent years, ~ 15.5% of mini perovskite module (size~40 cm²) produced by spraying process are reported [72]. Until now, efficiency of spray-coated PSCs still lags behind a meniscus-coated PSC due to nonuniform crystallization of perovskite and film coverage issue when one-step process is applied.

2.1.4 Inkjet printing coating

The inkjet printing method can reduce the procedure of the laser etching processing for module fabrication. For inkjet printing of the perovskite films, most inkjet-printed demonstrations utilize piezoelectric MEMs print heads, which provide controllable microfluidic jetting through a silicon-etched nozzle. To improve the reliability and the speed of printing, multiple jet nozzles are also devised [79]. Inkjet printing enables specific cell shapes for particular functions, such as small-scale utility power and building-integrated photovoltaics (BIPVs). Additionally, an essential advantage of continuous and other inkjet printing systems is that they do not require physical contact or critical gaps between the jet and the substrate, making them suitable for printing on uneven, curved, or pressure-sensitive surfaces [68]. It will also enable the printing of solar cells ideal for cars, especially esthetics, in the future. Saule Technologies uses this method for 1-m-wide perovskite in building-integrated photovoltaics (BIPVs) and EV charging ports. Thus, it is a very scalable technique for fabricating PSCs.

2.2 Solvent

Many papers have explained the growth mechanism of perovskite crystals in solvent [80, 81]. The interaction between solvents and perovskite compositions is significant in the nucleation and crystallization processes during the perovskite film formation. Noted that the choice of solvent in perovskite solution should consider how well solvent can dissolve precursors and crystallize them in a one-step method, as mentioned earlier. Polar aprotic solvents (DMF, DMSO, γ -butyrolactone (GBL), pyrrolidone (NMP), and acetonitrile (ACN)) are commonly used solvents. Organic

Fabrication method	Structure	Type	Method (solvent)	Condition	Area	PCE (%)	Ref
Slot-die (all layers)	ITO/ SnO ₂ /CsFAMAPbI ₃ -xBrx/Spiro	S2S	One step (DMF/DMSO/ additives)	ambient	0.07 cm ²	14.5	[69]
Slot-die (only perovskite)	ITO/TiO ₂ /CH ₃ NH ₃ PbI ₃ – xCl/Spiro	S2S	One step (DMF)	glove box	168.75 cm ²	11.1	[70]
Slot-die (SnO ₂ , perovskite)	PET/ITO/SnO ₂ / Cs _{0.15} FA _{0.85} .PbI _{2.85} Br _{0.15} / Spiro	R2R	One step (DMSO, 2BE)	ambient	0.04cm ² width 30 cm	13.5	[71]
Spray (TiO ₂ , perovskite)	ITO/TiO ₂ /CH ₃ NH ₃ PbI ₃ – xCl/PTAA	S2S	One step (DMF, GBL)	ambient	40 cm ²	15.5	[72]
Ultrasonic spray (all layers)	ITO/SnO ₂ Cs _{0.05} FA _{0.81} MA _{0.14} PbI _{2.55} Br _{0.45} I/ Spiro	S2S	One step (DMF/DMSO)	glove box	15.4mm ²	16.3	[73]
Inkjet printing (only PbI ₂)	FTO/TiO ₂ /MAPbI ₃ /Spiro/	S2S	Two step (DMF, DMSO)	ambient glove box	0.04 cm ²	18.3	[74]
Inkjet printing (all layers)	FTO/NiO/CsFAMAPbIBr/PCBM/	S2S	One step	glove box	10.5mm ²	16.5	[75]
Bar coating (only perovskite)	FTO/TiO ₂ /(FAPbI ₃) _{0.95} (MAPbBr ₃) _{0.05} / passivation/Spiro	S2S	One step (2ME/CHP)	ambient	31cm ²	17.53	[76]
Vacuum thermal evaporation (only perovskite)	FTO/TiO ₂ /MA _{1-x} Cs _x PbI ₃ /Spiro	S2S	Co-evaporation (MAI treatment)	ambient	9 mm ²	20.13	[77]
Vacuum thermal evaporation (all layers)	ITO/Ca/C60/perovskite/TAPC/TAPC:MoO ₃ /MoO	S2S	Sequentially evaporation	vacuum	0.1cm ²	17.6	[78]

Table 2.
Comparisons of some work by fabrication.

halides are relatively well soluble in organic solvents compared to metal halides (see **Table 2**). Many researchers prepare perovskite inks by dissolving organic halides into the DMF-based solvent before lead halides often decrease solvation time. The solvent has physical properties, such as Hansen's solubility parameters, dielectric constant, and Gutmann's donor number (DN). Solvents with dielectric constants more than 30 show generally good solubility for the perovskite precursors. In addition, halide in the solvents with low DN dominates the coordination with Pb^{2+} , and perovskites are quickly crystallized. In contrast, solvents with high DN compete for the coordination of I^- with Pb^{2+} slow down the crystallization of perovskites. Then higher DN solvents can be employed as solvent additives to control the crystallization of perovskite [82, 83]. However, by combining volatile non-coordinating solvents, i.e. 2-methoxy ethanol (2ME), and low volatile, coordinating solvent, i.e. N-cyclohexyl-2-pyrrolidone (CHP), Seok groups obtained bar-coated PSCs cells with a PCE of 20% with the area of 31 cm^2 [76]. 2ME has no or much weaker coordination capability. Thus, coordination ability and volatility (such as the boiling point and vapor pressure) can be critical parameters for perovskite crystallization. This solvent engineering will be a powerful technology for the scalability of printing. The toxicity of solvents, such as toxic DMF, skin-penetrating DMSO, or carcinogenic NMP, is also an important point, especially for operators who have direct contact with volatile solvents in the printing process [82]. It is difficult to determine whether 2ME is a commercially useful solvent or not due to the different regulations on industrial safety standards in country. On the other hand, DMSO is most environmentally friendly and least harmful to human health by systematically considering solvent production. Therefore, the search "green" solvent systems could also be critical for safe printing production [84].

2.3 Vacuum thermal evaporation-based fabrication of PSCs

Although vacuum thermal evaporation studies are relatively scarce, the following improvements led to PSCs with a PCE of 20%, not bad compared to the result of spin-coated PSCs (see **Table 2**) [77]. It was a significant result since there would be a feasible route to produce PSCs commercially, as proven by the CIGS and OLED industry. Next, we briefly summarize vacuum thermal evaporation-based fabrication methods.

2.3.1 Co-evaporation

This method is the most suitable vacuum-based process for many applications. The perovskite films are fabricated inside a high vacuum at a pressure of $10^{-5} \sim 10^{-6}$ bar. Each perovskite precursor is loaded into a crucible and heated to an appropriate sublimation temperature (**Figure 9(h)**). Removing the annealing step enables to deposit perovskite on any underlayer material [ref]. Perovskite films prepared in this way are more homogeneous, with better adherence to substrates than those prepared by spin coating. In addition, they are denser and pinhole-free, thus, more compatible with planar solar cells [85]. However, the most critical step is to control volatile organic halide (e.g. MAI) within the chamber, because it causes the compound to condense incompletely outside the evaporation cone region. The process is relatively slow and requires accurate periodic calibration to maintain deposition rates and precise stoichiometry.

2.3.2 Sequential evaporation

The method involves depositing several film layers sequentially on top of each other and then converting these multiple film layers through diffusion and recrystallization. The metal halide layer is typically deposited first and then converted by the organic halides. This method may not be ideal for optimal commercial scaling due to its throughput. By optimizing the system's pressure for each evaporation step, high efficiency of 17.6% was achieved in a small area. [78] This technique can be challenging to commercial scale as alternating evaporation can slow throughput and material utilization. When using a large vacuum chamber, the relatively long distance between the source and the substrate reduces the deposition rate and increases material waste. In addition, the vacuum-based fabrication of PSCs uses a variety of vapors, making control of the precursor stoichiometry challenging. The vacuum-based technology tends to be costly because of the sophisticated infrastructures required. However, major display companies such as Samsung and LG are converting their small- and medium-sized OLED panel manufacturing technology from the sixth generation (1500x1850 mm) to the eighth generation (2200 x 2500 mm). The evaporator and Fink Metal Mask (FMM) in a micrometer are the key to OLED panel production: The evaporator is critical equipment that forms red, green, and blue pixels, and FMM is a thin metal plate with small fine holes to induce the OLED material to be deposited on the substrate's required position. In addition, a curved display has also been developed. The curvature of curved TVs on the market today is roughly between 2000R and 4000R. The radius of curvature (R) is the reciprocal of the curvature. For example, 2000R TV refers to a curved TV radius of 2000 mm, and the lower R, the more pronounced curve, and the higher R, the more subtle curve. For mobile solar cell, the area of the panoramic sunroof in the vehicle is smaller than that of the 6Gen or 8Gen display. For example, the Hyundai YF sonata has a sunroof of 1000 x 1800 mm and a curvature of about 8125R (length) and 2512R (width). The vacuum deposition method applies to flexible substrates, metal foils, and ultrathin glass substrates with a thickness of 0.7 mm, so the range of solar application in a car is also wide

3. Summary

Perovskite solar cells have become one of today's most promising photovoltaic technologies. In this book, as the first section, we have introduced a lead-free CsSnI_3 and a stable molecular iodosalts, Cs_2SnI_6 , and demonstrated that it is a vapor-processable semiconductor. Due to the instability properties of CsSnI_3 , this research put more effort to develop Cs_2SnI_6 . The use of a new class structural material with intrinsic stability and beneficial optoelectronic properties can be considered as a start of the next chapter in perovskite photon devices. As the second section, large-area applicable perovskite coating technologies for commercialization were overhauled. PSCs based on the solution process can be manufactured at a much lower cost than conventional silicon cells as well as showing similar efficiency to silicon cells. However, to apply and commercialize this in real life, it needs a large-scale production technology while maintaining high efficiency. Until now, spin coating is the main technique. However, in general, this process has cracks or pinholes in the film when the coating area is expanded, resulting in poor density and uniformity. In addition, there is a limitation to reduce the amount of discarded solution, and it is difficult to do continuous (in-line) production. With increasing

demand for mass production, production of M6-sized PSCs module has been many technological advances. Plus, improving stability is a problem that must be solved. For long-term reliability of PSCs, various encapsulation processes are also being studied. By overcoming many issues that perovskite can have, our company plans to integrate the PSCs to vehicles by 2025.

Acknowledgements

This work was supported by Hyundai Motor Group project (R-204696).


Author details

Rira Kang[†], Tae-ho Jeong[†] and Byunghong Lee^{†*}
Electronic Device Team, Hyundai Motor Group, Uiwang-si, Gyeonggi-do, Korea

*Address all correspondence to: redboho@gmail.com

† These authors contributed equally.

IntechOpen

© 2022 The Author(s). Licensee IntechOpen. This chapter is distributed under the terms of the Creative Commons Attribution License (<http://creativecommons.org/licenses/by/3.0>), which permits unrestricted use, distribution, and reproduction in any medium, provided the original work is properly cited. 

References

- [1] NREL chart. Available from: <https://www.nrel.gov/pv/cell-efficiency.html>
- [2] Mitzi DB et al. Conducting tin halides with a layered organic-based perovskite structure. *Nature*. 1994;**369**(6480): 467-469
- [3] Hao F et al. Lead-free solid-state organic-inorganic halide perovskite solar cells. *Nat Photon*. 2014;**8**(6):489-494
- [4] Noel NK et al. Lead-free organic-inorganic tin halide perovskites for photovoltaic applications. *Energy & Environmental Science*. 2014;**7**(9): 3061-3068
- [5] Ogomi Y et al. CH₃NH₃Sn_xPb(1-x)I₃ perovskite solar cells covering up to 1060 nm. *The Journal of Physical Chemistry Letters*. 2014;**5**(6):1004-1011
- [6] Hao F et al. Anomalous band gap behavior in mixed Sn and Pb perovskites enables broadening of absorption Spectrum in solar cells. *Journal of the American Chemical Society*. 2014;**136**(22):8094-8099
- [7] Zuo F et al. Binary-metal perovskites toward high-performance planar-heterojunction hybrid solar cells. *Advanced Materials*. 2014;**26**(37): 6454-6460
- [8] Lee B et al. Air-stable molecular semiconducting Iodosalts for solar cell applications: Cs₂SnI₆ as a hole conductor. *Journal of the American Chemical Society*. 2014;**136**(43): 15379-15385
- [9] Chung I et al. CsSnI₃: Semiconductor or metal? High electrical conductivity and strong near-infrared photoluminescence from a single material. High hole mobility and phase-transitions. *Journal of the American Chemical Society*. 2012;**134**(20): 8579-8587
- [10] Lee B et al. Solution processing of air-stable molecular semiconducting iodosalts, Cs₂SnI_{6-x}Br_x, for potential solar cell applications. *Sustainable Energy & Fuels*. 2017;**1**(4): 710-724
- [11] Shum K et al. Synthesis and characterization of CsSnI₃ thin films. *Applied Physics Letters*. 2010;**96**(22): 221903
- [12] Fraiwan LF, et al. A wireless home safety gas leakage detection system. In: *Biomedical Engineering (MECBME), 2011 1st Middle East Conference on 2011*. 2011
- [13] Kumar MH et al. Lead-free halide perovskite solar cells with high photocurrents realized through vacancy modulation. *Advanced Materials*. 2014;**26**(41):7122-7127
- [14] Chen Z et al. Photoluminescence study of polycrystalline CsSnI₃ thin films: Determination of exciton binding energy. *Journal of Luminescence*. 2012;**132**(2):345-349
- [15] Sabba D et al. Impact of anionic Br-Substitution on open circuit voltage in Lead free perovskite (CsSnI_{3-x}Br_x) solar cells. *The Journal of Physical Chemistry C*. 2015;**119**(4):1763-1767
- [16] Stoumpos CC, Malliakas CD, Kanatzidis MG. Semiconducting tin and Lead iodide perovskites with organic cations: Phase transitions, high Mobilities, and near-infrared Photoluminescent properties. *Inorganic Chemistry*. 2013;**52**(15):9019-9038

- [17] Brik MG, Kityk IV. Modeling of lattice constant and their relations with ionic radii and electronegativity of constituting ions of A_2XY_6 cubic crystals ($a=K, Cs, Rb, Tl$; $X=tetravalent\ cation$, $Y=F, Cl, Br, I$). *Journal of Physics and Chemistry of Solids*. 2011;**72**(11): 1256-1260
- [18] Singh D. *Planewaves, Pseudopotentials, and the LAPW Method*. Boston, MA: Kluwer Academic; 1994
- [19] Kohn W, Sham LJ. Self-consistent equations including exchange and correlation effects. *Physical Review*. 1965;**140**(4A):A1133-A1138
- [20] Hohenberg P, Kohn W. Inhomogeneous Electron gas. *Physical Review*. 1964;**136**(3B):B864-B871
- [21] Perdew JP, Burke K, Ernzerhof M. Generalized gradient approximation made simple. *Physical Review Letters*. 1996;**77**(18):3865-3868
- [22] Koelling DD, Harmon BN. A technique for relativistic spin-polarised calculations. *Journal of Physics C: Solid State Physics*. 1977;**10**(16):3107
- [23] Blaha P et al. *An Augmented Plane Wave + Local Orbitals Program for Calculating Crystal Properties*. Austria: Universität Wien; 2001, Wien, Austria: Karlheinz Schwarz, Techn
- [24] Tran F, Blaha P. Accurate band gaps of semiconductors and insulators with a Semilocal exchange-correlation potential. *Physical Review Letters*. 2009; **102**(22):226401
- [25] Jeon NJ et al. Solvent engineering for high-performance inorganic-organic hybrid perovskite solar cells. *Nature Materials*. 2014;**13**(9): 897-903
- [26] Saparov B et al. Thin-film deposition and characterization of a Sn-deficient perovskite derivative Cs_2SnI_6 . *Chemistry of Materials*. 2016;**28**(7): 2315-2322
- [27] Fuchizaki K et al. Polyamorphism in tin tetraiodide. *The Journal of Chemical Physics*. 2009;**130**(12):121101
- [28] Fuchizaki K. Melting behavior of SnI_4 reexamined. *The Journal of Chemical Physics*. 2013;**139**(24):244503
- [29] Patterson AL. The Scherrer formula for X-ray particle size determination. *Physical Review*. 1939;**56**(10):978-982
- [30] Xiao Z et al. Solvent annealing of perovskite-induced crystal growth for photovoltaic-device efficiency enhancement. *Advanced Materials*. 2014;**26**(37):6503-6509
- [31] Qian W et al. Improving field emission by constructing CsI-AlN hybrid nanostructures. *Journal of Materials Chemistry*. 2012;**22**(35):18578-18582
- [32] Weiss M et al. Preparation and characterization of methylammonium tin iodide layers as photovoltaic absorbers. *Physica status solidi (a)*. 2016; **213**(4):975-981
- [33] Xiao Z et al. Intrinsic defects in a photovoltaic perovskite variant Cs_2SnI_6 . *Physical Chemistry Chemical Physics*. 2015;**17**(29):18900-18903
- [34] Dang Y et al. Formation of hybrid perovskite tin iodide single crystals by top-seeded solution growth. *Angewandte Chemie*. 2016;**128**(10): 3508-3511
- [35] Wells AF. *Structural Inorganic Chemistry*. Oxford University Press; 2012

- [36] Apostolico L et al. The reaction of tin (iv) iodide with phosphines: Formation of new halotin anions. Dalton Transactions. 2009;**47**:10486-10494
- [37] Apostolico L et al. The reaction of GeCl₄ with primary and secondary phosphines. Dalton Transactions. 2004;**3**:470-475
- [38] Guan J, Tang Z, Guloy AM. [H₃N(CH₂)₇NH₃]₈(CH₃NH₃)₂Sn(IV)Sn(II)I₂I₄ - a mixed-valent hybrid compound with a uniquely templated defect-perovskite structure. Chemical Communications. 2005;**1**:48-50
- [39] De Trizio L et al. Sn cation Valency dependence in cation exchange reactions involving Cu_{2-x}Se nanocrystals. Journal of the American Chemical Society. 2014;**136**(46):16277-16284
- [40] Lufaso MW, Woodward PM. Prediction of the crystal structures of perovskites using the software program SPuDS. Acta Crystallographica Section B. 2001;**57**(6):725-738
- [41] Xiao Z. First-Principles Study on Electronic Structure and Doping for Novel Compound Semiconductors, BaZn₂As₂, SnS, and Cs₂SnI₆. 2015
- [42] Goldschmidt VM. Die Gesetze der Krystallochemie. Naturwissenschaften. 1926;**14**(21):477-485
- [43] Li Z et al. Stabilizing perovskite structures by tuning tolerance factor: Formation of Formamidinium and cesium Lead iodide solid-state alloys. Chemistry of Materials. 2016;**28**(1): 284-292
- [44] Lee B, Buchholz DB, Chang RPH. An all carbon counter electrode for dye sensitized solar cells. Energy & Environmental Science. 2012;**5**(5): 6941-6952
- [45] Kim H-S et al. Mechanism of carrier accumulation in perovskite thin-absorber solar cells. Nature Communications. 2013;**4**
- [46] Gonzalez-Pedro V et al. General working principles of CH₃NH₃PbX₃ perovskite solar cells. Nano Letters. 2014;**14**(2):888-893
- [47] Xing G et al. Long-range balanced Electron- and hole-transport lengths in organic-inorganic CH₃NH₃PbI₃. Science. 2013;**342**(6156):344-347
- [48] Lee B et al. Materials, interfaces, and photon confinement in dye-sensitized solar cells. The Journal of Physical Chemistry B. 2010;**114**(45):14582-14591
- [49] Lee B et al. Optimizing the performance of a plastic dye-sensitized solar cell. The Journal of Physical Chemistry C. 2011;**115**(19):9787-9796
- [50] Garcia-Belmonte G et al. Charge carrier mobility and lifetime of organic bulk heterojunctions analyzed by impedance spectroscopy. Organic Electronics. 2008;**9**(5):847-851
- [51] Fabregat-Santiago F et al. Characterization of nanostructured hybrid and organic solar cells by impedance spectroscopy. Physical Chemistry Chemical Physics. 2011;**13**(20):9083-9118
- [52] Leever BJ et al. In situ characterization of lifetime and morphology in operating bulk heterojunction organic photovoltaic devices by impedance spectroscopy. Advanced Energy Materials. 2012;**2**(1): 120-128
- [53] Nagpal P, Klimov VI. Role of mid-gap states in charge transport and photoconductivity in semiconductor

- nanocrystal films. *Nature Communications*. 2011;**2**:486
- [54] Margulies EA et al. Enabling singlet fission by controlling intramolecular charge transfer in π -stacked covalent terrylenediimide dimers. *Nature Chemistry*. 2016 advance online publication
- [55] Liu Q et al. Exciton relaxation dynamics in photo-excited CsPbI₃ perovskite nanocrystals. *Scientific Reports*. 2016;**6**:29442
- [56] Wang L et al. Femtosecond time-resolved transient absorption spectroscopy of CH₃NH₃PbI₃ perovskite films: Evidence for passivation effect of PbI₂. *Journal of the American Chemical Society*. 2014;**136**(35):12205-12208
- [57] Makarov NS et al. Spectral and dynamical properties of single excitons, Biexcitons, and Trions in cesium–Lead-halide perovskite quantum dots. *Nano Letters*. 2016;**16**(4):2349-2362
- [58] Piatkowski P et al. Direct monitoring of ultrafast electron and hole dynamics in perovskite solar cells. *Physical Chemistry Chemical Physics*. 2015; **17**(22):14674-14684
- [59] Cherepy NJ et al. Ultrafast Electron injection: Implications for a Photoelectrochemical cell utilizing an anthocyanin dye-sensitized TiO₂ Nanocrystalline electrode. *The Journal of Physical Chemistry B*. 1997;**101**(45): 9342-9351
- [60] Perovskite info. Available from: <https://www.perovskite-info.com/companies>
- [61] Liu F et al. Organic solar cells with 18% efficiency enabled by an alloy acceptor: A two-in-one strategy. *Advanced Materials*. 2021;**33**(27): 2100830
- [62] Zhao Y et al. Research progress in large-area perovskite solar cells. *Photonics Research*. 2020;**8**(7):A1-A15
- [63] Li J et al. Optimization of anti-solvent engineering toward high performance perovskite solar cells. *Journal of Materials Research*. 2019; **34**(14):2416-2424
- [64] Gu X et al. The meniscus-guided deposition of semiconducting polymers. *Nature Communications*. 2018;**9**(1):534
- [65] Dai X et al. Meniscus fabrication of halide perovskite thin films at high throughput for large area and low-cost solar panels. *International Journal of Extreme Manufacturing*. 2019
- [66] Deng Y et al. Tailoring solvent coordination for high-speed, room-temperature blading of perovskite photovoltaic films. *Science. Advances*. 2019;**5**(12):eaax7537
- [67] Kim YY et al. Roll-to-roll gravure-printed flexible perovskite solar cells using eco-friendly antisolvent bathing with wide processing window. *Nature Communications*. 2020;**11**(1):5146
- [68] Hamukwaya SL et al. A review of recent developments in preparation methods for large-area perovskite solar cells. *Coatings*. 2022;**12**(2):252
- [69] Xu Z et al. Nanocrystal-enabled front-surface bandgap gradient for the reduction of surface recombination in inverted perovskite solar cells. *Solar RRL*. 2021;**5**(10):2100489
- [70] Di Giacomo F et al. Up-scalable sheet-to-sheet production of high efficiency perovskite module and solar cells on 6-in. Substrate using slot die

- coating. *Solar Energy Materials and Solar Cells*. 2018;**181**:53-59
- [71] Galagan Y et al. Roll-to-roll slot die coated perovskite for efficient flexible solar cells. *Advanced Energy Materials*. 2018;**8**(32):1801935
- [72] Heo JH et al. Highly efficient CH₃NH₃PbI₃-xCl_x mixed halide perovskite solar cells prepared by re-dissolution and crystal grain growth via spray coating. *Journal of Materials Chemistry A*. 2016;**4**(45):17636-17642
- [73] Bishop JE et al. Fully spray-coated triple-cation perovskite solar cells. *Scientific Reports*. 2020;**10**(1):6610
- [74] Li Z et al. Ink engineering of inkjet printing perovskite. *ACS Applied Materials & Interfaces*. 2020;**12**(35):39082-39091
- [75] Schackmar F et al. Perovskite solar cells with all-inkjet-printed absorber and charge transport layers. *Advanced Materials Technologies*. 2021;**6**(2):2000271
- [76] Yoo JW et al. Efficient perovskite solar mini-modules fabricated via bar-coating using 2-methoxyethanol-based formamidinium lead tri-iodide precursor solution. *Joule*. 2021;**5**(9):2420-2436
- [77] Zhu X et al. Superior stability for perovskite solar cells with 20% efficiency using vacuum co-evaporation. *Nanoscale*. 2017;**9**(34):12316-12323
- [78] Hsiao S-Y et al. Efficient all-vacuum deposited perovskite solar cells by controlling reagent partial pressure in high vacuum. *Advanced Materials*. 2016;**28**(32):7013-7019
- [79] Swartwout R, Hoerantner MT, Bulović V. Scalable deposition methods for large-area production of perovskite thin films. *Energy & Environmental Materials*. 2019;**2**(2):119-145
- [80] Nayak PK et al. Mechanism for rapid growth of organic-inorganic halide perovskite crystals. *Nature Communications*. 2016;**7**(1):13303
- [81] Ono LK, Juarez-Perez EJ, Qi Y. Progress on perovskite materials and solar cells with mixed cations and halide anions. *ACS Applied Materials & Interfaces*. 2017;**9**(36):30197-30246
- [82] Wang Y et al. Printing strategies for scaling-up perovskite solar cells. *National Science Review*. 2021;**8**(8)
- [83] Hamill JC, Schwartz J, Loo Y-L. Influence of solvent coordination on hybrid organic-inorganic perovskite formation. *ACS Energy Letters*. 2018;**3**(1):92-97
- [84] Park SH, Jin IS, Jung JW. Green solvent engineering for environment-friendly fabrication of high-performance perovskite solar cells. *Chemical Engineering Journal*. 2021;**425**:131475
- [85] Hamukwaya SL et al. A review of recent developments in preparation methods for large-area perovskite solar cells. *Coatings*. 2022